A compact six-port dielectric resonator antenna array: MIMO channel measurements and performance analysis

Tian, Ruiyuan; Plicanic, Vanja; Lau, Buon Kiong; Ying, Zhinong

A Compact Six-Port Dielectric Resonator Antenna Array: MIMO Channel Measurements and Performance Analysis

Ruiyuan Tian, *Student Member, IEEE,* Vanja Plicanic, *Member, IEEE,* Buon Kiong Lau, *Senior Member, IEEE,* and Zhinong Ying, *Senior Member, IEEE*

Abstract—MIMO systems ideally achieve linear capacity gain proportional to the number of antennas. However, the compactness of terminal devices limits the number of spatial degrees of freedom (DOFs) in such systems, which motivates efficient antenna design techniques to exploit all available DOFs. In this contribution, we present a compact six-port dielectric resonator antenna (DRA) array which utilizes spatial, polarization and angle diversities. To evaluate the proposed DRA array, a measurement campaign was conducted at $2.65\,\mathrm{GHz}$ in indoor office scenarios for four 6×6 multiple antenna systems. Compared to the reference system of monopole arrays which only exploit spatial diversity, the use of dual-polarized patch antennas at the transmitter enriches the channel's DOF in the non-line-of-sight scenario. Replacing the monopole array at the receiver with the DRA array that has a 95% smaller ground plane, the 10% outage capacity evaluated at $10\,\mathrm{dB}$ reference signal-to-noise ratio becomes equivalent to that of the reference system, due to the DRA's rich diversity characteristics. In the line-of-sight scenario, the DRA array gives a higher DOF than the monopole array as the receive counterpart to the transmit patch array. However, the outage capacity is $1.5\,\mathrm{bits/s/Hz}$ lower, due to the DRA array's lower channel gain.

Index Terms—MIMO systems, dielectric resonator antennas, polarization, antenna diversity.

I. INTRODUCTION

MIMO systems can achieve high spectrum efficiency in wireless communications by employing multiple antennas at both the transmit (TX) and receive (RX) sides. Such systems perform best when the spatial correlation among signals on different antenna branches is low [1]. However, the compactness of today's terminal devices limits the degrees of freedom (DOFs), and consequently the correlation performance in such systems. This motivates the need for efficient design techniques to exploit all available DOFs. Recent examples on the design and performance evaluation of compact multiple antenna terminals include [2]–[4].

In 1938, Richtmyer showed that a suitably shaped dielectric material can function as electrical resonators for high frequency oscillations [5]. The characteristics of such dielectric resonators have been the subject of many early studies, *e.g.*, [5]–[7]. More recently, their application as antenna elements has been demonstrated [8]–[10]. One interesting feature of dielectric resonator antennas (DRAs) is that the antenna can be electrically small (at the expense of efficiency bandwidth) when high permittivity material is used. This makes it attractive for compact implementations in wireless communications. In [11], a low profile single-port L-shape DRA fed by a planar inverted-F antenna (PIFA) is designed for laptop in Wireless LAN (WLAN) applications. In [12], a compact cylindrical DRA is designed for triple-mode operation, where two modes are excited for radiation in two different frequency bands, and the third mode is used as a filter. In [13]–[16], a single three-port rectangular DRA element is developed and evaluated for diversity and MIMO antenna systems in WLAN-type applications. Most of the existing studies focus on the antenna performance of scattering parameters and radiation patterns, and they do not consider the effect of the propagation channel. In [17], the single three-port DRA proposed in [13] is evaluated with ray tracing simulations of an indoor environment, and it is shown to achieve comparable capacity performance as a conventional uniform linear array of ideal dipoles despite its significantly more compact size. Even though the ray tracing simulations in [17] can give an initial indication of the DRA's performance in its usage environment, they utilize simplifying assumptions of the modeled 3D environment and the propagation mechanisms. Therefore, measurements in real environments are crucial to fully substantiate the DRA's practicality.

In this contribution, we propose a diversity-rich yet compact six-port antenna array. The proposed array consists of two three-port DRA elements, which jointly utilizes spatial, polarization and angle diversities. In order to evaluate its performance for WLAN-type applications, a 6×6 MIMO channel measurement campaign was conducted at $2.65\,\mathrm{GHz}$ in indoor scenarios. Two common types of six-port antenna arrays were also measured in the campaign for the purpose of comparison: a single-polarized monopole array exploiting only spatial diversity, and a dual-polarized patch array exploiting spatial and polarization diversities. The measurement results are analyzed in order to demonstrate the potential use of the compact DRA array for MIMO communications, in comparison to the larger monopole and patch arrays.

The reminder of paper is structured as follows. Section II describes the measurement campaign in detail. Section III
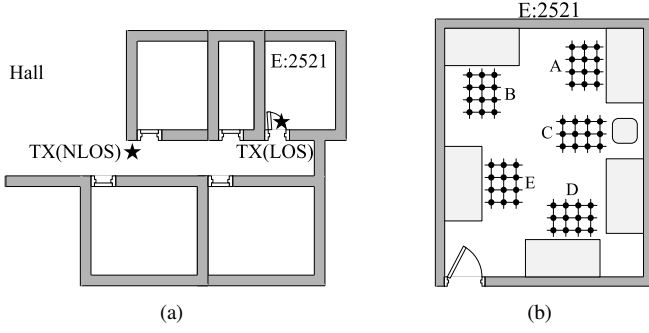
Fig. 1. Floor map of the measurement campaign. (a) TX antenna array positions marked by black stars. (b) Room E:2521 with RX antenna array positions marked by black dots. The light gray rectangles are the office desks.

presents the characteristics of the three types of six-port antenna arrays used in this study. In Section IV, the performance of array dependent measured MIMO channels are evaluated and analyzed. Section V concludes the discussion.

II. MEASUREMENT CAMPAIGN

A. Setup

The channel transfer functions between the TX/RX antenna pairs were measured using the RUSK LUND wideband channel sounder, which performs MIMO channel measurements based on the "switched array" principle [18]. The measurements were performed using 321 subcarrier signals over 200 MHz bandwidth with a center frequency at 2.65 GHz. However, we only used the measured data over 100 MHz bandwidth (*i.e.*, 2.6 GHz − 2.7 GHz) for this study. The output power of the channel sounder was 0.5 W (27 dBm). The length of the test signal to obtain one snapshot (in time) for one TX-RX channel branch was set to be 1.6 μs, which ensured long enough "excess runlength" of multipath components to avoid overlap of subsequent impulse responses in the considered environment [19]. A block of 20 consecutive snapshots was obtained for each RX measurement position (of a given array orientation). The measured channel matrices obtained from the consecutive snapshots are used in post processing to enhance the signal-to-noise ratio (SNR) of the measurement and to estimate the noise power.

B. Scenario

The channel measurements were performed in a corridor and office room E:2521 on the second floor of the E-building at LTH, Lund University, Sweden, as shown in Figure 1. The dimensions of the room are 5.7 m (length)×4.9 m (width)×3.0 m (height). There were desks, chairs, a large white board, and other typical office furniture in the room.

The RX unit of the channel sounder was stationed at the end of the corridor, which is just outside room E:2521 during the entire measurement campaign. The RX antenna array, placed on top of a trolley at the height of an office desk (*i.e.*, 0.7 m), was stationed at different measurement locations inside the office (see Figure 1(b)). In total, 5 rectangular grids of measurement positions (A - E) were chosen in proximity of the desks. Within each grid, 12 positions were measured in

order to obtain good fading statistics. Adjacent measurement positions within each grid were two wavelengths (226 mm at 2.65 GHz) apart from each other. At each measurement position, two orientations of the RX array were performed. The array was rotated 90 ° horizontally with respect to the orientation in the first measurement to obtain the second measurement set. For both orientations, the rectangular ground plane of the RX array was aligned in parallel with the office walls, *i.e.*, in the first (second) orientation, the longer side of the array's ground plane was aligned in parallel with the longer (shorter) side of the office room.

Two propagation scenarios were measured: line-of-sight (LOS) and non-line-of-sight (NLOS). In the NLOS scenario, the TX antenna array was located 9.7 m away from the end of corridor (see Figure 1(a)). The TX unit of the channel sounder was stationed in the hall area behind the TX antenna array. In the LOS scenario, the TX and RX array structures are in LOS of each other. The TX antenna was located next to the door inside the office, whereas the TX unit of the channel sounder was stationed outside the office. It is further noted that even though the TX and RX array *structures* are in LOS, the LOS path may not necessarily exist between the TX and RX array *elements*, depending on the orientation of the TX array. The effect of LOS obstruction will be examined in Section IV. In both scenarios, the TX antenna array was placed at a height of 1.8 m, corresponding to the height of an elevated WLAN Access Point (AP).

The following steps were taken in order to minimize disturbances and assure a static measurement environment: (1) The MIMO channel was measured for the center frequency of 2.65 GHz, instead of 2.45 GHz, in order to avoid interference from the existing WLAN systems while maintaining similar propagation characteristics. Furthermore, a spectrum analyzer was used to ensure no detectable interfering sources in the measured environment. WLAN APs in proximity of the measured site were disabled during the measurement. (2) The measurement campaign was conducted during one occasion, from late one afternoon to early next morning. No significant movement within the measurement site during the campaign was ensured. After each measurement run, a person either rotated the RX antenna array or moved it to the next position for the next measurement. (3) The doors of other offices along the corridor were closed. (4) Absorber units were used to cover the body of the TX/RX unit of the channel sounder.

III. ANTENNA CONFIGURATIONS

The measurement campaign comprises the evaluation of four TX/RX multiple antenna systems, listed in Table I.

Using sparsely separated single-polarized monopoles at both TX and RX antenna systems, Case I represents a reference system for WLAN-type applications. This is due to the well-known characteristics of monopole antennas. In addition, the antenna spacing between monopoles is designed to be one wavelength to minimize coupling and spatial correlation. In Case II, dual-polarized patch antennas are used at the TX subsystem to exploit polarization diversity and to characterize polarized propagation. In Case III, the proposed DRA array is
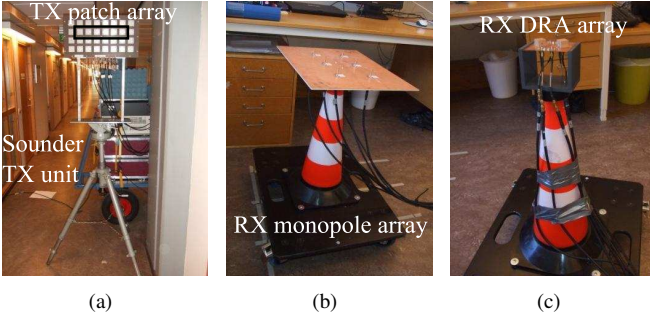
Fig. 2. Photos of (a) the TX patch antenna array on a tripod in the NLOS scenario; (b) the RX monopole antenna array; (c) the RX DRA array.
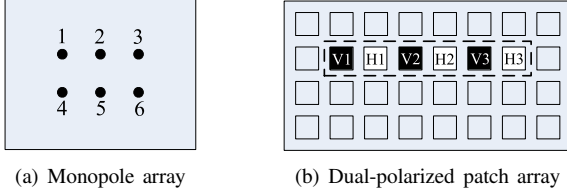

(a) Monopole array (b) Dual-polarized patch array

Fig. 3. Sketches of (a) the monopole and (b) the patch antenna arrays.

(a) $G_i(\theta = 90°, \phi)$ [dBi], $i = 1, \ldots, 6$

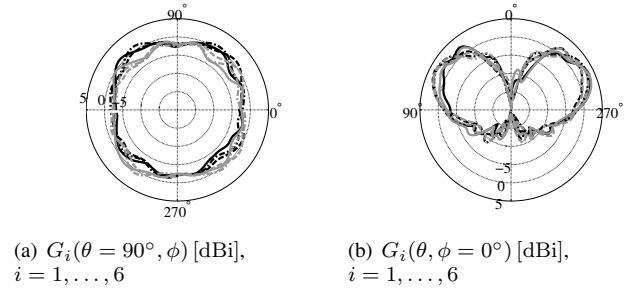(b) $G_i(\theta, \phi = 0°)$ [dBi], $i = 1, \ldots, 6$

Fig. 4. Measured realized gain patterns G [dBi] of the six-port monopole antenna array at 2.65 GHz.

(a) (b)

Fig. 5. (a) Simulation model of the compact DRA array. (b) Drawing of the single DRA prototype.

investigated at the RX subsystem, such that the RX antenna system is physically compact (*e.g.*, wireless terminals). In this system, the patch array is chosen as the TX counterpart since it is able to excite propagation in two orthogonal polarizations, and is thus a suitable match for the multi-polarized DRA array. In addition, the compact DRA array is evaluated against the monopole array at the RX end by comparing Cases II and III. In Case IV, the compact DRA array is used at both TX and RX antenna systems. This case corresponds to a more compact design of the TX antenna system, *i.e.*, the WLAN AP.

Details of the antenna arrays are given below. The monopole and DRA arrays were evaluated with a vector network analyzer and in a Satimo Stargate measurement system [20]. The DRA was also simulated with the CST software [21]. The specifications of the patch array are available in [22].

A. Monopole Array

The monopole array consists of six vertical quarter-wavelength ($\lambda/4$) monopole antennas spaced one wavelength (113 mm at 2.65 GHz) apart from one another in a rectangular grid on a ground plane (see Figures 2(b) and 3(a)). The ground plane size is 460×345 mm^2.

The monopole array covers the evaluated frequency band of 2.6 GHz − 2.7 GHz. The reflection coefficient is less than −19 dB, and the coupling between the neighboring elements is less than −20 dB. The antenna total efficiency, taking into account mismatch, dielectric and conductive losses, is 82 %.

TABLE I
LIST OF ANTENNA SYSTEMS UNDER EVALUATION.

Case	TX antenna array	RX antenna array
I	Vertically polarized monopoles	Vertically polarized monopoles
II	Dual-polarized patches	Vertically polarized monopoles
III	Dual-polarized patches	Tri-polarized DRAs
IV	Tri-polarized DRAs	Tri-polarized DRAs
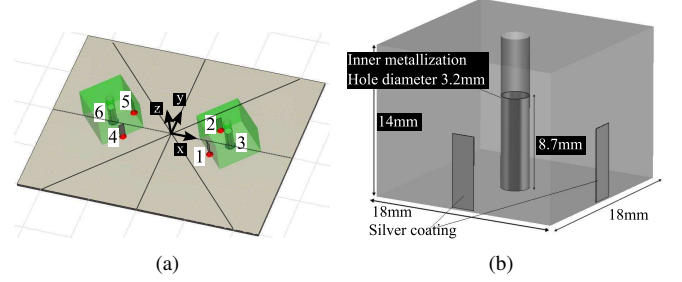
on average. The measured realized gain patterns are given in Figure 4. Approximately uniform patterns are observed in the azimuth plane for all elements of the array. In the elevation plane, however, the maximum gain of 5 dBi is obtained at 30° above the azimuth plane, due to the finite ground plane size [23]. The impact of the elevated radiation patterns on measured channel characteristics is examined in Section IV.

During the measurement of Cases I and II, the ground planes of the monopole arrays were placed horizontally such that the monopole elements were vertically polarized.

B. Patch Array

The patch array [22] is a uniform planar array with 4×8 dual-polarized radiating square patch elements (64 ports in total) spaced half a wavelength (56.6 mm at 2.65 GHz) apart in a rectangular grid (see Figure 2(a)). For the 6×6 MIMO channel measurements, six patch elements in a row were chosen, such that the $\{1, 3, 5\}$-th elements were vertically polarized and the $\{2, 4, 6\}$-th elements were horizontally polarized. All other ports were terminated with 50 Ω loads. A sketch of the antenna array is shown in Figure 3(b).

The patch antenna array has a reflection coefficient of less than −12 dB within the 2.6 GHz − 2.7 GHz frequency band. The coupling between adjacent co-polarized elements is less than −11 dB. For the cross-polarized ports on the same patch element, the polarization isolation is more than 23 dB. The antenna total efficiency is approximately 83 %, with a maximum gain of 6.6 dBi.

To take into consideration the patch antennas' radiation characteristics in Cases II and III, the patch elements were facing the end of the corridor in the NLOS scenario and into room E:2521 in the LOS scenario (see Figure 1).
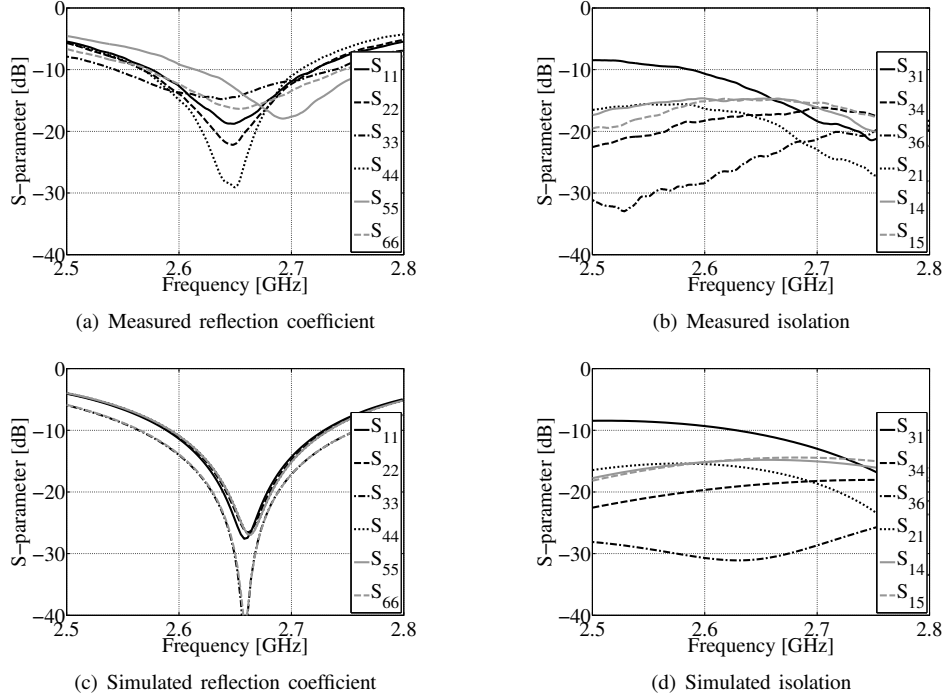
(a) Measured reflection coefficient

(b) Measured isolation

(c) Simulated reflection coefficient

(d) Simulated isolation

Fig. 6.   Measured and simulated S-parameters of the compact DRA array.

C. Compact DRA Array

The compact DRA array consists of two three-port DRA elements placed with reflection symmetry (see Figures 2(c) and 5). Each DRA element comprises a cube of open dielectric material on a ground plane. Two microstrip excitation ports are on the sides and a monopole port is in the middle of the structure. A rectangular dielectric resonator theoretically supports two fundamental TE-modes which radiate like magnetic dipoles [10]. The two silver microstrips on two perpendicular faces of the cube are used to excite these modes. A monopole antenna is inserted into the center of the dielectric resonator to create a third port without disturbing the radiating modes of the dielectric resonator.

Figure 5(a) shows the simulation model of the compact six-port DRA array that is tuned to the center frequency of $2.65\,\mathrm{GHz}$. Ports $\{1,2\}$ and $\{4,5\}$ denote the microstrip excitation ports, and ports 3 and 6 denote the monopole ports on the two DRA elements, respectively. The dimensions of the single DRA element are given in Figure 5(b). The dielectric resonator cube, which is obtained from TDK, has relative permittivity $(\varepsilon_{\mathrm{r}})$ of 19.6 and a loss tangent $(\tan\delta)$ of 0.0001352. At the center frequency of $2.65\,\mathrm{GHz}$, the electrical dimensions of each dielectric resonator cube are $0.16\lambda \times 0.16\lambda \times 0.12\lambda$ and the monopole has a length of 0.08λ. The separation distance between the center of the two DRA elements is $50\,\mathrm{mm}$ (0.44λ). The ground plane size of the DRA array is $100 \times 80\,\mathrm{mm}^2$, *i.e.*, 95% smaller compared to the monopole array. The compactness makes the proposed DRA array an attractive candidate for use in wireless terminals. It should be noted that the sizes of both the DRA element and the DRA array can be further reduced for specific terminal devices, if required. However, the prototype used suffices as a proof of concept for the suitability of DRA arrays for MIMO communications in an indoor environment.

Figure 6 shows the S-parameters of the DRA array obtained from both measurements and simulations (using CST software [21]). As can be seen, the DRA array covers the $100\,\mathrm{MHz}$ frequency band at $2.65\,\mathrm{GHz}$ with a reflection coefficient of less than $-10\,\mathrm{dB}$. The measured and simulated results agree well, except for some minor detuning observed in the measured port 5. The worst isolation of $10\,\mathrm{dB}$ is observed between a given microstrip excitation port and the monopole port on the same DRA element (*e.g.*, between ports $\{1,2\}$ and 3). The isolation between all other ports is more than $15\,\mathrm{dB}$. The S-parameters that are not shown exhibit similar behavior due to the symmetrical structure of the DRA array.

The measured radiation patterns of the compact DRA array are shown in three different cuts: one ϕ-plane $(\theta = \pi/2)$ in Figure 7, and two θ-planes $(\phi = 45°, 135°)$ in Figures 8 and 9. The two θ-planes are chosen to be aligned with the vertical faces of the DRA elements (see Figure 5(a)). First, reflection symmetry is observed between the patterns of the two antenna elements. The six radiation patterns of the two DRAs are directed towards a broad range of distinct directions. For example, the two monopole patterns (ports 3 and 6) provide coverage in opposite directions (*i.e.*, compare subplots (e) and (f) in Figures 7-9). Since different antenna ports primarily see different directions, angle diversity can be achieved. Second, polarization diversity is also exploited. In Figure 7, the monopole patterns (ports 3 and 6) have a stronger contribution in the θ-component, whereas the two polarizations (θ- and ϕ-components) are orthogonal across the patterns of the microstrip excitation ports (ports $\{1,2,4,5\}$). Moreover, as shown in Figure 8 for the $(\theta, \phi = 45°)$-cut, the
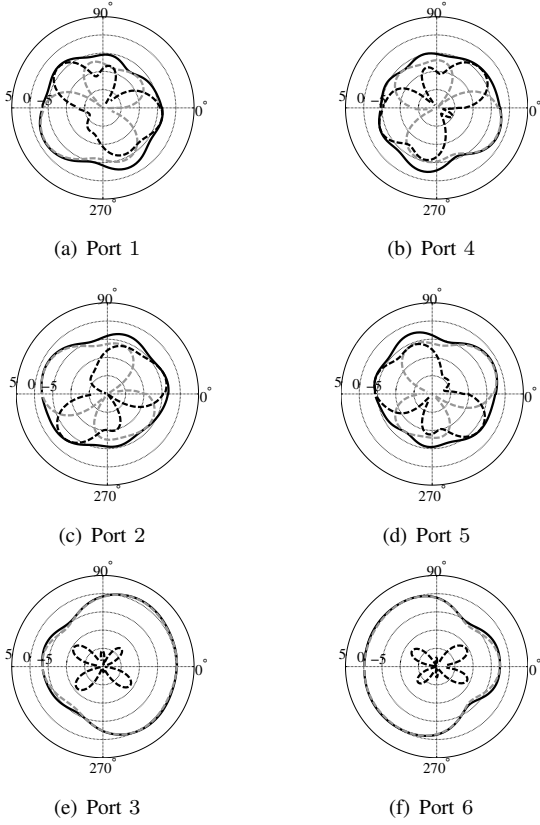
Fig. 7. Measured realized gain patterns $G(\theta = 90°, \phi)$ [dBi] of the six-port compact DRA array at $2.65\,\text{GHz}$. Black solid line: total gain; Light gray dashed line: θ-component; Black dashed line: ϕ-component.

Fig. 8. Measured realized gain patterns $G(\theta, \phi = 45°)$ [dBi] of the six-port compact DRA array at $2.65\,\text{GHz}$. Black solid line: total gain; Light gray dashed line: θ-component; Black dashed line: ϕ-component.

patterns of ports 1 and 5 are dominated by the θ-component, whereas the patterns of ports 2 and 4 are dominated by the ϕ-component. The diverse radiation patterns make the compact DRA array robust to incoming waves with arbitrary directions and polarizations, thus making good use of the available DOF.

The simulated radiation patterns are in good agreement with the measured ones, and are not included here due to space constraint. Nevertheless, the simulations gave the insight that the strong currents are concentrated under the DRA elements and around the microstrip excitation ports when the TE-modes are excited. When the monopole is excited, the strong currents mainly reside on the monopole element. Thus, no significant radiation is associated with the ground plane. The DRA array has an antenna total efficiency of $68\,\%$ on average, with a maximum gain of $5.1\,\text{dBi}$. During the measurement of Cases III and IV, the ground plane of the RX DRA array was placed horizontally. However, the ground plane of the TX DRA array in Case IV was placed vertically, in order to account for the array's radiation characteristics.

IV. ANALYSIS

In this section, the measured MIMO channels for the four antenna systems are evaluated and analyzed. The investigated parameters include RX power, SNR, branch power ratio (BPR), channel envelope distribution and MIMO performance in terms of channel capacity.
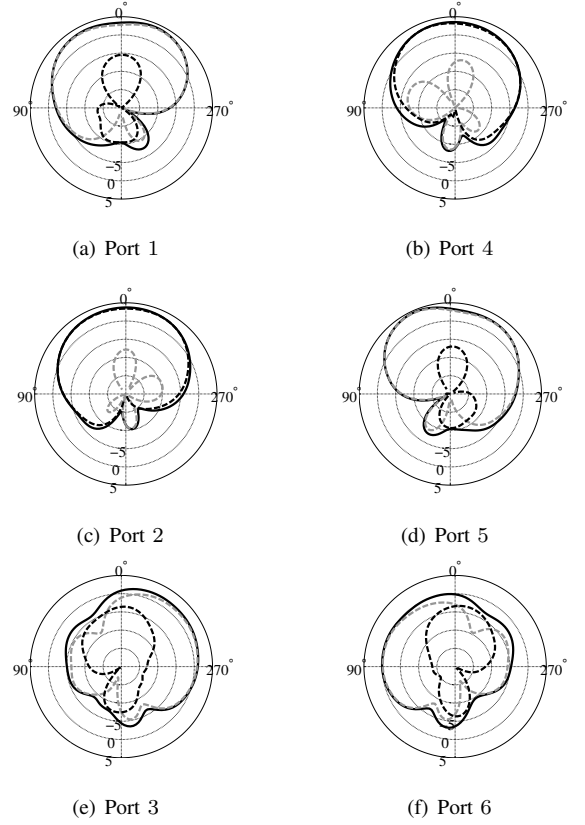
A. RX Power

The RX power is calculated from the measured MIMO channel matrices of each evaluated antenna system $\mathbf{H}_{s,l}^{(n)}, \{1 \leq s \leq S, 1 \leq l \leq L, 1 \leq n \leq N\}$, as

$$P_{\text{RX},s,l} = \frac{1}{N} \sum_{n=1}^{N} ||\mathbf{H}_{s,l}^{(n)}||_{\text{F}}^2, \tag{1}$$

where $|| \cdot ||_{\text{F}}$ denotes the Frobenius norm operator, $S = 4$ denotes the number of measured antenna systems (Cases I - IV), $L = 5$ is the number of measured grid positions (A - E), and $N = 161 \times 12 \times 2$ is the number of narrowband channel realizations obtained from 161 frequency subcarriers (*i.e.*, within $2.6\,\text{GHz} - 2.7\,\text{GHz}$) at 12 measured points within each grid and with two array orientations.

The RX power of all other antenna systems under evaluation (Cases II - IV) are compared to that of the reference system (Case I). Table II summarizes the relative RX power averaged among the five measured grids. Case II collects significantly more power on average ($4.1\,\text{dB}$ in LOS and $1.6\,\text{dB}$ in NLOS) than other cases. The strong channel gain is due to the patch and the monopole array having the highest antenna efficiency and gain at the TX and RX subsystems, respectively. In addition, the orientation of the TX patch array makes Case II favorable for a higher RX power, since the maximum gain is directed towards the general direction of the RX array. In Case I, however, the finite ground plane of the TX monopole array makes the radiation pattern elevated such that the maximum
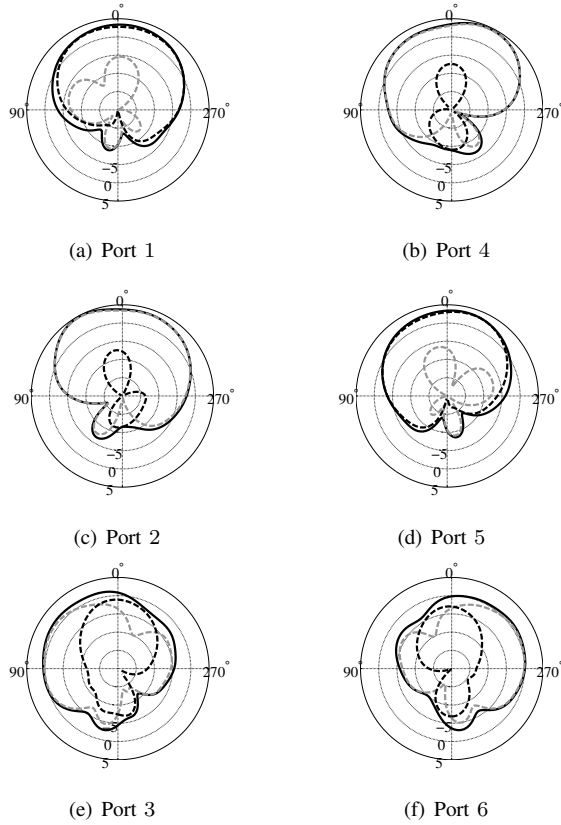
(a) Port 1   (b) Port 4

(c) Port 2   (d) Port 5

(e) Port 3   (f) Port 6

Fig. 9. Measured realized gain patterns $G(\theta, \phi = 135°)$ [dBi] of the six-port compact DRA array at 2.65 GHz. Black solid line: total gain; Light gray dashed line: θ-component; Black dashed line: ϕ-component.
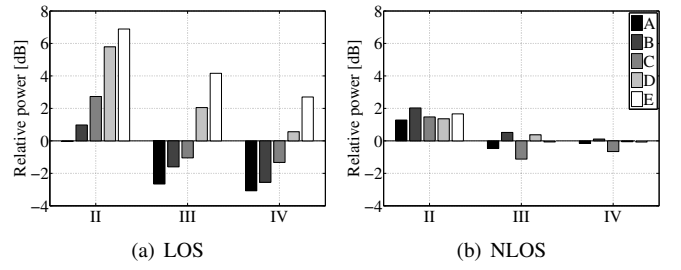

(a) LOS   (b) NLOS

Fig. 10. Averaged RX power relative to Case I of each antenna system (Cases II - IV) at each measurement grid position (A - E).

(a) Case I   (b) Case II

(c) Case III   (d) Case IV
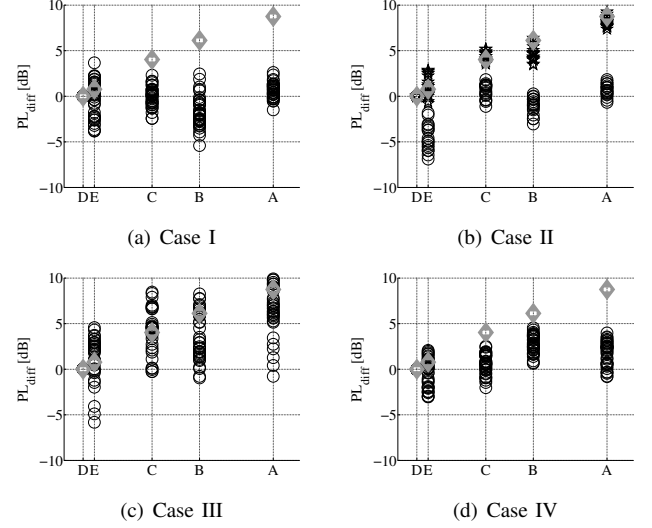
Fig. 11. Path loss of each antenna system (Cases I - IV) at each measurement grid position in the LOS scenario. {A,B,C,D,E} denote the distance (in linear scale) from the TX array to the center of each measured grid. Grid D is used as a reference position. Gray diamonds: path loss model; Black circles and stars: measured channel branches.

gain is directed away from the RX antennas. Cases III and IV exhibit channel gains of within 1 dB relative to that of the reference system.

Figure 10 illustrates the relative RX power of Cases II - IV with respect to Case I measured at each grid position (A - E), in LOS and NLOS scenarios, respectively. In LOS, see Figure 10(a), a trend of increasing RX power from grid positions A to E is observed. In order to further study this effect, a simple path loss model [24] is used

$$\overline{PL}(d)\,[\text{dB}] = \eta \times 10\log_{10}(d), \qquad (2)$$

where $\overline{PL}(d)$ denotes the path loss, d denotes the TX-RX separation distance, and η is the path loss exponent. Denoting grid position D, which is closest to the TX array position (see Figure 1(b)), as a reference distance d_0, the path loss difference $\overline{PL}_{\text{diff}}$ is found for other measured grid positions, as

$$\overline{PL}_{\text{diff}} = \overline{PL}(d) - \overline{PL}(d_0). \qquad (3)$$

Figure 11 compares the path loss difference obtained from the measured RX power of each channel branch with the

TABLE II
AVERAGED RX POWER RELATIVE TO CASE I.

Case	LOS	NLOS
II	4.1 dB	1.6 dB
III	1.0 dB	−0.1 dB
IV	−0.2 dB	−0.2 dB

calculation using Equation (3) with $\eta = 2.5$. While the increase of path loss is partly due to the increase of the TX-RX separation, the measured RX power is also strongly influenced by the choice of antenna systems. Specifically, the RX power in Case I is approximately invariant to the change in TX-RX separation distance (see Figure 11(a)). For Case II, a closer examination reveals that the RX power of the co-polarized channel branches (indicated by stars in Figure 11(b)) agree with the path loss model, whereas this is not the case for the cross-polarized channel branches (indicated by circles). These effects are further investigated in the following sections.

B. SNR

The SNRs of the measured channels are estimated using the 20 consecutive snapshots obtained at each measurement location and array orientation. Since the measured channel at each location is supposed to be static as described in Section II, the differences between the measured channel matrices obtained from the consecutive snapshots are used to estimate the noise power (or variance). On average, the SNR is found to be 27.4 dB in LOS and 23.1 dB in NLOS.

(a) Case I, LOS

(b) Case I, NLOS

(c) Case II, LOS

(d) Case II, NLOS

(e) Case III, LOS

(f) Case III, NLOS

(g) Case IV, LOS

(h) Case IV, NLOS

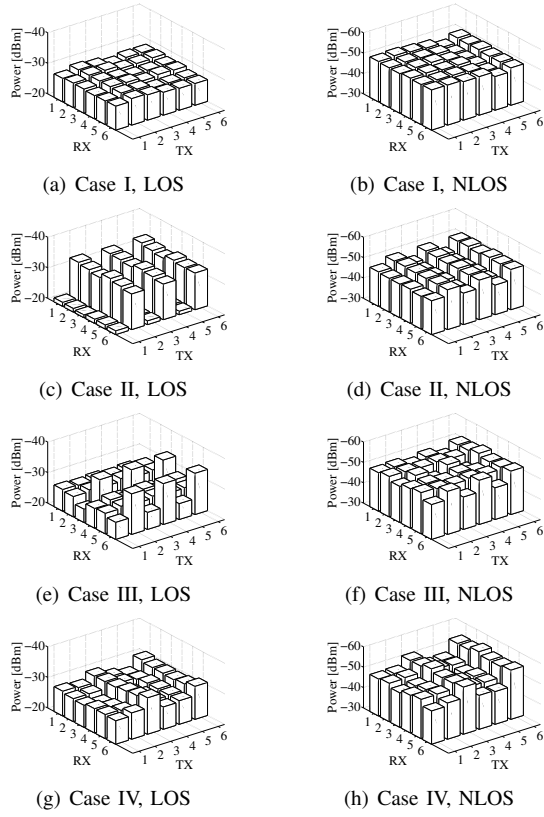Fig. 12. Averaged RX power for each TX/RX antenna pair, in total of 36 channel branches. Note the negative sign on y-axis, *i.e.*, the higher the box the less the power.

C. Branch Power Ratio

In order to investigate the branch power of each TX/RX antenna pair, Figure 12 illustrates the averaged RX power of each TX/RX channel (*i.e.*, 36 channel branches in total) for all antenna systems (Cases I - IV) in LOS and NLOS.

1) Case I: As shown in Figures 12(a) and 12(b), the RX power in the reference system (Case I) is approximately uniformly distributed among all channel branches. However, in other antenna systems (Cases II - IV), branch power imbalance is observed. Channel branches with distinct characteristics can be identified in groups, see Table III. The power ratios between different groups of channel branches are given in Table IV.

2) Case II: Figures 12(c) and 12(d) show that significant branch power imbalance is observed between vertically excited channels (TX ports $\{1, 3, 5\}$) and horizontally excited channels (TX ports $\{2, 4, 6\}$). The BPR is defined as the power ratio between co-polarized channels $\mathbf{H}_{\mathrm{mc}}$ and cross-polarized channels $\mathbf{H}_{\mathrm{mx}}$. In LOS, the direct propagation dominates so that the cross-polarization ratio (XPR) is inherently high. The co-polarized channels are found to be $11.3\,\mathrm{dB}$ stronger than the cross-polarized channels. In NLOS, the multipath propagation induces significant cross-polarization response. Thus, the BPR is reduced to $4.2\,\mathrm{dB}$.

3) Case III: Three groups of channel branches can be identified from Figures 12(e) and 12(f), according to the characteristics of the microstrip excitation and monopole ports on the RX DRA array. In LOS, the channel branches with co-polarized monopoles ($\mathbf{H}_{\mathrm{mc}}$) achieves about $8\,\mathrm{dB}$ higher power than the cross-polarized monopoles ($\mathbf{H}_{\mathrm{mx}}$), whereas the BPR of the channel branches with microstrip excitation ports ($\mathbf{H}_{\mathrm{p}}$) to the cross-polarized monopoles ($\mathbf{H}_{\mathrm{mx}}$) on the RX DRA array is about $5.9\,\mathrm{dB}$. In NLOS, branch power imbalance is mitigated and BPRs of $\mathbf{H}_{\mathrm{mc}}$ to $\mathbf{H}_{\mathrm{mx}}$ and $\mathbf{H}_{\mathrm{p}}$ to $\mathbf{H}_{\mathrm{mx}}$ are reduced to about $5\,\mathrm{dB}$ and $2\,\mathrm{dB}$, respectively. Compared to Case II, the BPR is reduced due to the RX DRA array exploiting polarization diversity. Thus, the compact DRA array is shown to be more robust in polarized propagation channels, but with $1.7 - 3.1\,\mathrm{dB}$ less of RX power (compare Cases II and III in Table II).

4) Case IV: Two groups of channel branches can be identified from Figures 12(g) and 12(h), according to the characteristics of the microstrip excitation and monopole ports on the TX DRA array. On the one hand, the TX DRA array is placed perpendicular with respect to the RX DRA array. This results in cross-polarized monopole elements in the corresponding TX/RX pairs. On the other hand, the microstrip excitation ports achieve higher gain than the monopole ports discussed in Section III-C. Consequently, the BPR is about $3.6\,\mathrm{dB}$ and $5.5\,\mathrm{dB}$ in LOS and NLOS, respectively. This can be understood by the rich angle diversity characteristics of the compact DRA array. The radiation patterns cover a broad range of directions such that branch power imbalance is mitigated in LOS.

D. Power Normalization

The above discussion on the RX power reveals that it is important to account for the impact of path loss in the normalization of the channel realizations. In this work, the measured channel matrices of each antenna system are normalized locally within each measurement grid. For channel matrices $\mathbf{H}_{s,l}^{(n)}, \{1 \leq s \leq S, 1 \leq l \leq L, 1 \leq n \leq N\}$, the

TABLE III
GROUPS OF CHANNEL BRANCHES.

Case II			
Group	TX ports	RX ports	Elements on RX monopole array
$\mathbf{H}_{\mathrm{mc}}$	$1, 3, 5$	$1, \ldots, 6$	Co-polarized monopoles
$\mathbf{H}_{\mathrm{mx}}$	$2, 4, 6$	$1, \ldots, 6$	Cross-polarized monopoles
Case III			
Group	TX ports	RX ports	Elements on RX DRA array
$\mathbf{H}_{\mathrm{p}}$	$1, \ldots, 6$	$1, 2, 4, 5$	Microstrip excitation ports
$\mathbf{H}_{\mathrm{mc}}$	$1, 3, 5$	$3, 6$	Co-polarized monopoles
$\mathbf{H}_{\mathrm{mx}}$	$2, 4, 6$	$3, 6$	Cross-polarized monopoles
Case IV			
Group	TX ports	RX ports	Elements on TX DRA array
$\mathbf{H}_{\mathrm{p}}$	$1, 2, 4, 5$	$1, \ldots, 6$	Microstrip excitation ports
$\mathbf{H}_{\mathrm{m}}$	$3, 6$	$1, \ldots, 6$	Monopoles

TABLE IV
BPR OF MEASURED ANTENNA SYSTEMS.

BPR [dB]		LOS	NLOS
Case II	$\mathbf{H}_{\mathrm{mc}}/\mathbf{H}_{\mathrm{mx}}$	11.3	4.2
Case III	$\mathbf{H}_{\mathrm{p}}/\mathbf{H}_{\mathrm{mx}}$	5.9	2.0
	$\mathbf{H}_{\mathrm{mc}}/\mathbf{H}_{\mathrm{mx}}$	8.0	5.0
Case IV	$\mathbf{H}_{\mathrm{p}}/\mathbf{H}_{\mathrm{m}}$	3.6	5.5

normalized MIMO channel matrices are obtained as [1]

$$\mathbf{H}_{\text{norm},s,l}^{(n)} = \mathbf{H}_{s,l}^{(n)} \left[\frac{1}{N N_{\text{T}} N_{\text{R}}} \sum_{n=1}^{N} ||\mathbf{H}_{s,l}^{(n)}||_{\text{F}}^2 \right]^{-1/2}. \quad (4)$$

N_{T} and N_{R} are the numbers of TX and RX antenna ports, respectively. With this approach, the small-scale power variation among the measured points within each grid is preserved, whereas the large-scale power variations and the differences in path loss between different grids are neglected. The following two normalization principles are considered:

1) Normalized RX SNR: (assuming power control) The measured channel matrices of each antenna system (Cases I - IV) are normalized independently, such that all antenna systems have the same average evaluation SNR at the RX side. Thus the channel's DOF can be investigated regardless of the relative power difference among the four antenna systems.

2) Case I as Reference: In order to account for the relative channel gain discussed in Section IV-A, the measured channel matrices of Cases II - IV are normalized with respect to the reference system (Case I). This is achieved by setting $s = 1$ inside $[\cdot]$ of Equation (4) for all the measured antenna systems.

E. Envelope Distribution

In order to obtain channel envelope distributions for all measured antenna systems, channel matrices are normalized according to the principle of Normalized RX SNR. The envelope distribution is found for each group of channel branches defined in Table III, respectively. The BPR is further removed by normalizing each group of channel branches independently.

Each of the measured envelope distributions is fitted to a theoretical cumulative distribution function (CDF) of Rician distribution using maximum likelihood estimation. The K-factor can be calculated as the power ratio between the dominant and the Rayleigh components [23]. In the measured NLOS scenario of all antenna systems, the Rician distribution reduces to Rayleigh, as the obtained K-factors approach 0. For LOS, Table V summarizes the K-factor of each antenna system obtained at each grid position in detail.

1) Case I: The Rician K-factors are negligibly small in the measured LOS scenario. This is mainly due to the elevated radiation patterns of the monopoles discussed in Section III-A. Moreover, since the RX and TX antennas are placed at different heights, the ground plane of the TX array obstructs the LOS path between the TX/RX array elements, which further restricts the number of dominant components and results in small K-factors in this particular LOS scenario.

TABLE V
ESTIMATED RICIAN K-FACTOR OF MEASURED CHANNELS IN LOS.

Grid position		A	B	C	D	E
Case I	$\mathbf{H}$	0.5	0	0.9	0	0.5
Case II	$\mathbf{H}_{\text{mc}}$	1.4	1.5	5.2	6.4	13.9
	$\mathbf{H}_{\text{mx}}$	0.2	0	0.5	1.3	0
Case III	$\mathbf{H}_{\text{p}}$	0	0.5	0	0.2	2.6
	$\mathbf{H}_{\text{mc}}$	0.5	0.5	0.4	2.3	2.5
	$\mathbf{H}_{\text{mx}}$	0	0	0.3	0.4	0
Case IV	$\mathbf{H}_{\text{p}}$	0.5	0.4	1.8	0.9	0.9
	$\mathbf{H}_{\text{m}}$	0	0	0	1.6	0

2) Case II: A clear distinction of the envelope distribution between co- and cross-polarized channels is observed in the measured LOS scenario. $\mathbf{H}_{\text{mc}}$ is described by Rician distributions with larger K-factors, which indicate the presence of dominant components. The obtained K-factor is found to be increasing from grid position A to E with decreasing TX/RX separation distance (see Table V), which implies that the corresponding increases in RX power observed in Section IV-A is mainly attributed to the increase in power of the dominant component. On the other hand, as indicated by the high BPR and XPR in Section IV-C, $\mathbf{H}_{\text{mx}}$ is described by negligibly small K-factors, suggesting a Rayleigh distribution.

3) Case III: In this case, although channel branches with cross-polarized monopoles ($\mathbf{H}_{\text{mx}}$) is described by Rician distribution with negligibly small K-factors, other channel branches show the presence of slightly more dominant components. In particular, in the extreme LOS scenario at measured grid position E, channel branches with microstrip excitation ports ($\mathbf{H}_{\text{p}}$) as well as co-polarized monopoles ($\mathbf{H}_{\text{mc}}$) on the RX DRA array exhibit relatively strong K-factors. Nevertheless, the dominant components are much less significant than those in Case II, as the obtained K-factors in Case II are 5 times greater than the corresponding ones in Case III. Recall that the BPR is also mitigated in Case III relative to Case II, which indicates that the tri-polarized DRA array is more robust in polarized channels than the monopole array.

4) Case IV: The K-factors of the two groups of channel branches are found to be small in the measured LOS scenario, which suggest that there is no significant dominant component. This can be understood by the mismatch in the array orientation mismatch of the TX/RX antenna pair, where the TX DRA array is oriented perpendicular to its RX counterpart. Moreover, the diverse radiation patterns of the DRA array cover a broad range of directions with different polarization contributions, which further reduce the number of direct propagation paths in LOS.

F. MIMO Capacity

The channel capacity is evaluated for the measured MIMO channels, assuming no channel knowledge at the TX end, *i.e.*, with equal TX power allocation. The capacity is evaluated at the SNR of $10\,\text{dB}$ (recall that the SNRs obtained from the measurements were higher than $20\,\text{dB}$). The measured channel matrices are normalized according to the two normalization principles discussed in Section IV-D.

Figure 13 shows CDF of the measured channel capacity of all four antenna systems, applying the two normalization principles, in NLOS and LOS, respectively. In subplots (a) and (c), the channel's DOF is compared with the 6×6 and 5×5 i.i.d. Rayleigh fading channels. Eigenvalue dispersion is also studied as a scale-invariant metric to describes the multipath richness and the channel's DOF [25], and similar findings are obtained. In subplots (b) and (d), the channel capacity of Cases II-IV are compared to the reference system.

1) Capacity I - Normalized RX SNR:

a) NLOS: Figure 13(a) shows that none of the evaluated antenna systems can achieve the performance of the 6×6

(a) NLOS, Normalized RX SNR

(b) NLOS, Case I as Reference

(c) LOS, Normalized RX SNR
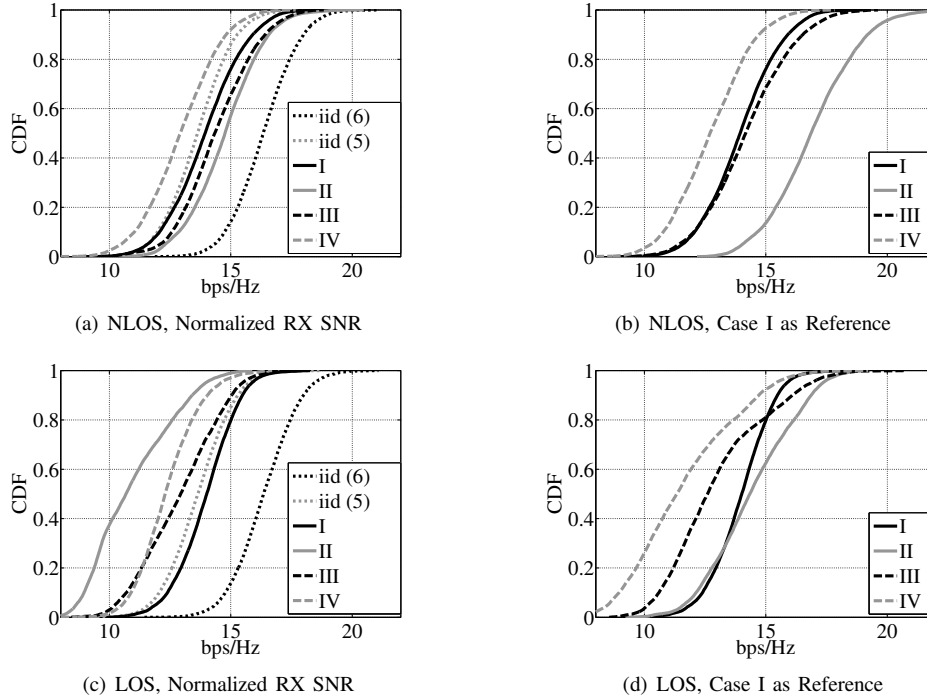
(d) LOS, Case I as Reference

Fig. 13. Cumulative distribution function (CDF) of measured MIMO channel capacity.

i.i.d. Rayleigh fading channel in NLOS. The reference system (Case I) that only exploits spatial diversity achieves a similar 10% outage capacity as the 5×5 i.i.d. Rayleigh channel. Case II achieves the best performance since both polarization and spatial diversities are exploited to enrich the channel's DOF. In Case III, the ground plane of the compact RX DRA array is 95% smaller than that of the RX monopole array in Case II, which restrics the available spatial diversity. However, the diversity-rich design of the DRA array employs polarization and angle diversities to achieve a similar DOF performance as that in Case II. In Case IV, the performance is worse than that of the 5×5 i.i.d. Rayleigh channel. This indicates that the channel's DOF is limited by the compact DRA array when it is used at both ends of the communication links.

b) LOS: In Figure 13(c), the reference system (Case I) and Case IV maintain similar performances as those in NLOS. However, for Case II, the performance decreases significantly compared to that in NLOS, and is the worst performance among all cases. This is attributed to the strong branch power imbalance observed in Section IV-C, where distinct channel envelope distributions are identified for the co- and cross-polarized channels. The Rician K-factor is found to be 14 for the co-polarization. Given the normalized RX SNR, the significant branch power imbalance is detrimental to the capacity and DOF performance. On the other hand, the high BPR and Rician K-factor is mitigated in Case III when the compact DRA array is employed at the RX subsystem. Thus, the robust performance of the compact DRA array also provides a better DOF performance than the RX monopole array in Case II.

2) Capacity II - Case I as Reference:

a) NLOS: When taking into account the relative power differences among the four antenna systems (see Figure 13(b)),

Case II achieves significantly better capacity performance, where the 10% outage capacity is $2.6 \, \mathrm{bits/s/Hz}$ higher than that of the reference system. The improved capacity relative to Figure 13(a) is due to its $1.6 \, \mathrm{dB}$ higher channel gain as discussed in Section IV-A. Case III achieves the same outage capacity as the reference system, since the DOF (Figure 13(a)) and the channel gain (Table II) is similar between Cases I and III in NLOS. Case IV has the worst outage capacity, which is $1.3 \, \mathrm{bits/s/Hz}$ lower than that of the reference system.

b) LOS: Figure 13(d) shows that Case II achieves a slightly lower outage capacity as that of the reference system. Although Case II has poorer DOF as shown in Figure 13(c), its performance is improved due to the $4.1 \, \mathrm{dB}$ higher channel gain. Case III gives $1.5 \, \mathrm{bits/s/Hz}$ lower 10% outage capacity compared to Case II, although the use of RX DRA array achieves higher DOF performance. This is due to its $3.1 \, \mathrm{dB}$ lower channel gain than Case II. In Case IV, the 10% outage capacity is $3.4 \, \mathrm{bits/s/Hz}$ lower than the reference system, due to both limited DOF and lower channel gain.

V. CONCLUSIONS

In this work, a compact six-port DRA array is proposed. In order to demonstrate its suitability for WLAN-type applications relative to common (but larger) array types, its performance is evaluated with measured MIMO channels of indoor office scenarios. Table VI summarizes the performance of the measured MIMO channels for the four different 6×6 multiple antenna systems.

Compared to the reference system using sparsely separated monopoles at the TX/RX subsystems, the use of dual-polarized patch antennas at the TX end and the proposed DRA array at the RX end shows rich characteristics of spatial, polarization

TABLE VI
SUMMARY OF PERFORMANCE.

		Case I	Case II	Case III	Case IV
TX antenna array		Mono.	Patch	Patch	DRA
RX antenna array		Mono.	Mono.	DRA	DRA
RX power	LOS	0	4.1	1	-0.2
[dB]	NLOS	0	1.6	-0.1	-0.2
BPR (max)	LOS	0	11.3	8.0	3.6
[dB]	NLOS	0	4.2	5.0	5.5
K-factor	LOS	0.9	13.9	2.6	1.8
(max)	NLOS	0	0	0	0
Capacity I	LOS	12.4	9.0	10.7	10.9
[bps/Hz]	NLOS	12.1	12.9	12.6	11.0
Capacity II	LOS	12.4	12.1	10.6	9.0
[bps/Hz]	NLOS	12.1	14.7	12.0	10.8

and angle diversities. The channel's DOF is found to be higher than that of the reference system in the measured NLOS scenario, which together with its slightly lower channel gain, results in similar channel capacity for the two cases.

In addition, the proposed DRA array is shown to be more robust than the monopole array as the RX counterpart to the TX patch array. It achieves a higher DOF than the RX monopole array in the measured LOS scenario, whose performance is shown to be limited due to the high BPR of the cross-polarized channels, as well as the strong Rician K-factor of the co-polarized channels. However, the achievable 10% outage capacity at $10\,\mathrm{dB}$ reference SNR is $1.5\,\mathrm{bits/s/Hz}$ lower. This is attributed to the $3.1\,\mathrm{dB}$ lower channel gain of the RX DRA array.

Furthermore, the antenna system with the proposed DRA array at both ends of the communication link is also evaluated. This corresponds to implementing compact multiple antenna solutions at both link ends. The penalty for implementing the compact TX array is the reduction in DOF, which results in $1.3\,\mathrm{bits/s/Hz}$ and $3.4\,\mathrm{bits/s/Hz}$ lower outage capacity than the reference system in NLOS and LOS, respectively.

REFERENCES

[1] M. Jensen and J. Wallace, "A review of antennas and propagation for MIMO wireless communications," *IEEE Trans. Antennas Propagat.*, vol. 52, no. 11, pp. 2810–2824, Nov. 2004.

[2] Y. Gao, X. Chen, Z. Ying, and C. Parini, "Design and performance investigation of a dual-element PIFA array at 2.5 GHz for MIMO terminal," *IEEE Trans. Antennas Propagat.*, vol. 55, no. 12, pp. 3433–3441, Dec. 2007.

[3] J. Villanen, P. Suvikunnas, C. Icheln, J. Ollikainen, and P. Vainikainen, "Performance analysis and design aspects of mobile-terminal multi-antenna configurations," *IEEE Trans. Veh. Technol.*, vol. 57, no. 3, pp. 1664–1674, May 2008.

[4] A. Diallo, C. Luxey, P. Le Thuc, R. Staraj, and G. Kossiavas, "Diversity performance of multiantenna systems for UMTS cellular phones in different propagation environments," *Int. J. Antennas Propagat.*, 2008.

[5] R. D. Richtmyer, "Dielectric resonators," *J. of Appl. Phys.*, vol. 10, no. 6, pp. 391–398, 1939.

[6] J. Van Bladel, "The excitation of dielectric resonators of very high permittivity," *IEEE Trans. Microwave Theory and Tech.*, vol. 23, no. 2, pp. 208–217, Feb. 1975.

[7] ——, "On the resonances of a dielectric resonator of very high permittivity," *IEEE Trans. Microwave Theory and Tech.*, vol. 23, no. 2, pp. 199–208, Feb. 1975.

[8] M. McAllister, S. Long, and G. Conway, "Rectangular dielectric resonator antenna," *Electron. Lett.*, vol. 19, no. 6, pp. 218–219, Mar. 1983.

[9] A. Kishk, H. Auda, and B. Ahn, "Accurate prediction of radiation patterns of dielectric resonator antennas," *Electron. Lett.*, vol. 23, no. 25, pp. 1374–1375, Dec. 1987.

[10] R. K. Mongia and A. Ittipiboon, "Theoretical and experimental investigations on rectangular dielectric resonator antennas," *IEEE Trans. Antennas Propagat.*, vol. 45, no. 9, pp. 1348–1356, Sep. 1997.

[11] W. Huang and A. Kishk, "A DRA fed by PIFA for laptop WLAN application," in *Proc. IEEE Antennas Propagat. Soc. Int. Symp., San Diego, CA*, Jul. 2008.

[12] L. Hady, D. Kajfez, and A. Kishk, "Triple mode use of a single dielectric resonator," *IEEE Trans. Antennas Propagat.*, vol. 57, no. 5, pp. 1328–1335, May. 2009.

[13] Z. Ying, "Compact dielectric resonant antenna," *U.S. Patent Application No. 20080122703*, Sep. 22, 2006.

[14] K. Ishimiya, J. Långbacka, Z. Ying, and J.-i. Takada, "A compact MIMO DRA antenna," in *Proc. Int. Workshop Antenna Technol. (IWAT 2008), Chiba, Japan*, Mar. 4-6 2008, pp. 286–289.

[15] K. Ishimiya, Z. Ying, and J.-i. Takada, "A compact MIMO DRA for 802.11n application," in *Proc. IEEE Antennas Propagat. Soc. Int. Symp., San Diego, CA*, Jul. 2008.

[16] N. Oland, "WLAN MIMO terminal test in reverberation chamber," Master's thesis, Chalmers University of Technology, Gothenburg, Sweden, 2008. [Online]. Available: http://publications.lib.chalmers.se/records/fulltext/70869.pdf

[17] I. Shoaib, Y. Gao, K. Ishimiya, X. Chen, and Z. Ying, "Performance evaluation of the 802.11n compact MIMO DRA in an indoor environment," in *Proc. 3rd Europ. Conf. Antennas Propagat., (EuCAP 2009), Berlin, Germany*, Mar. 23-27, 2009.

[18] R. Thoma, D. Hampicke, A. Richter, G. Sommerkorn, A. Schneider, U. Trautwein, and W. Wirnitzer, "Identification of time-variant directional mobile radio channels," *IEEE Trans. Instrum. Meas.*, vol. 49, no. 2, pp. 357–364, Apr. 2000.

[19] J. Kåredal, A. Johansson, F. Tufvesson, and A. Molisch, "A measurement-based fading model for wireless personal area networks," *IEEE Trans. Wireless Commun.*, vol. 7, no. 11, pp. 4575–4585, Nov. 2008.

[20] "SATIMO homepage." [Online]. Available: http://www.satimo.fr

[21] "CST Computer Simulation Technology AG homepage." [Online]. Available: http://www.cst.com

[22] Ö. Isik, "Planar and cylindrical microstrip array antennas for MIMO-channel sounder applications," Master's thesis, Chalmers University of Technology, Gothenburg, Sweden, 2004.

[23] R. Vaughan and J. B. Andersen, *Channels, Propagation and Antennas for Mobile Communications*. London: The IEE, 2003.

[24] T. S. Rappaport, *Wireless Communications: Principles and Practice*. New Jersey: Prentice Hall PTR, 1996.

[25] J. Salo, P. Suvikunnas, H. El-Sallabi, and P. Vainikainen, "Ellipticity statistic as measure of MIMO multipath richness," *Electronics Letters*, vol. 42, no. 3, pp. 160–162, Feb. 2006.